



LAWRENCE
LIVERMORE
NATIONAL
LABORATORY

LLNL-TR-655174

Implementation of mechanical model for shale

A. V. Attia, O. Y. Vorobiev, S. D. Walsh

June 2, 2014

Disclaimer

This document was prepared as an account of work sponsored by an agency of the United States government. Neither the United States government nor Lawrence Livermore National Security, LLC, nor any of their employees makes any warranty, expressed or implied, or assumes any legal liability or responsibility for the accuracy, completeness, or usefulness of any information, apparatus, product, or process disclosed, or represents that its use would not infringe privately owned rights. Reference herein to any specific commercial product, process, or service by trade name, trademark, manufacturer, or otherwise does not necessarily constitute or imply its endorsement, recommendation, or favoring by the United States government or Lawrence Livermore National Security, LLC. The views and opinions of authors expressed herein do not necessarily state or reflect those of the United States government or Lawrence Livermore National Security, LLC, and shall not be used for advertising or product endorsement purposes.

This work performed under the auspices of the U.S. Department of Energy by Lawrence Livermore National Laboratory under Contract DE-AC52-07NA27344.

Implementation of mechanical model for shale

Armand Attia, Oleg Vorobiev and Stuart Walsh

June 2, 2014

LLNL-TR-655174

This work was performed under the auspices of the U.S. Department of Energy by Lawrence Livermore National Laboratory under Contract DE-AC52-07NA27344.

1 Introduction

Modeling of fracture of shales during drilling and hydraulic fracturing is a major research area for gas and oil industries [1, 2, 3, 4].

Due to their laminate structure, shales exhibit an anisotropic mechanical response which has been ignored for long time. Yet, recently there have been a few attempts to develop and use orthotropic models for shales [5, 4].

The purpose of this report is to identify published rock material models and properties that can help a petroleum engineer in his design of various strategies for oil/gas recovery from shale rock formation. Drilling strategies may include using explosives for fracturing rock and injection of proppants for maintaining fractures open. During drilling, borehole stability is an important concern, requiring an understanding of natural shale layered structure, elastic moduli, strength, pore fluid pressure, mineral content, etc

To account for the layered shale structure, which can be on a very small scale, an anisotropic model is necessary to calculate rock response to applied loading. Where explosives are used to break up the rock, porosity and compaction need to be modeled, and the model needs to be sensitive to relatively high strain rate. Far away from the explosion site, the rock is subject to lower strain rates, so that strain-rate sensitivity is not an issue.

A petroleum engineer has a variety of tools at his disposal in developing his strategy. These tools include measuring rock properties (logging) at various depths, extracting rock samples for laboratory measurements (e.g. triaxial tests). To evaluate borehole stability, techniques may range, for example, from calculating borehole collapse pressure using analytical models [6] to FEM codes that incorporate constitutive models, such as [5]. Both types of techniques require validation with experimental data. The focus of this report will be mainly on constitutive models (used in FEM codes) using parameters that can be calibrated to rock tests, and a collection of available data for such tests. The Crook model [5] has been identified as a complete anisotropic model that can be used as a good starting point.

In this report, we review several approaches to modeling shale and then focus on the implementation of a particular model (the Crook anisotropic model).

2 Models applied to blast loading

The first papers will illustrate capabilities and limitations of isotropic models used to calculate rock behavior under explosive loading. Grady and Kipp in [7], Kipp and Grady in [8], Kipp, Grady, Chen in [9] show good agreement between experimental and analytical results finding that fracture stress and energy increase with strain rate while fragment size decreases with strain rate, using only isotropic damage models. However, Taylor, Chen, Kuszmaul in [10] find that isotropic models with or without layering are only able to reproduce the peak values of measured stress waves but not the release history.

Zhang, Hao, Lu in [11] argue that an anisotropic damage model is needed

but their results for fracture stress and fragment size are just as good as those obtained by Grady et al, in the previous papers, for the same data.

3 Models applied to triaxial tests

The next set of papers apply various anisotropic formulations to triaxial tests.

Nova [12] assumes linear transverse isotropic elasticity, with an anisotropic yield, associative plastic flow, and strain-hardening, in an extended cam-clay model, intended for soft rocks. While the model gives good agreement with experiment for longitudinal stiffness, triaxial test simulations do not agree well with experimental data. Specifically, the model gives poor agreement with experiment for stress-difference (S_1-S_3) vs. strain.

Niandou et al [13] were able to correct this deficiency in Nova's model by allowing for non-associative flow (with a plastic potential distinct from the yield) in order to match their Tournemire shale data [14].

Cazacu and Cristescu [15] developed a failure model, based on an anisotropic Mises-Schleicher failure criterion, which agrees very well with Tournemire data for the variation of failure stress with orientation and for various confining pressures, where the orientation angle is defined for the principal stress system with respect with the material symmetry structural system. They also present an anisotropic model [2] in which they use extensive fitting to formulate elastic parameters and a yield surface. The expression for the yield surface is initially unknown and is fully determined from experimental data.

Tien [16] studies the failure stress of artificially layered material. He introduces a failure criterion based on two modes of failure: sliding on a discontinuity across material layers and failure within a single layer without sliding. Tien identifies an anisotropy parameter n defined by:

$$n = \frac{E}{2G} - \nu \quad (1)$$

which is equal to 1 for isotropic material. E is Young's modulus at 90 degrees with respect to the intrinsic material frame and G and ν are the shear modulus and Poisson's ratio, in the same frame. For Martinsburg shale, he finds that this parameter varies only from 3.5 to 4.6 over confining pressures ranging widely from 3.5 MPa to 100 MPa. He obtains good agreement for the Tournemire data.

Pietruszczak et al[17] develops an intricate anisotropic model with microstructure without damage, which shows moderate agreement for stress difference vs. volumetric strain for the Tournemire data.

Gao et al [18] present an anisotropic failure criterion, in which they introduce a fabric tensor to achieve some success in the calculation of the friction angle, giving clearly better results than an isotropic model. Their model does quite well on Tournemire shale, predicting correctly the variation in shear strength for various loading orientations. They provide a calibration procedure for the parameters introduced in the failure criterion. Note that they do not present the entire model, but only the failure criterion.

Chen et al [19] also introduce a fabric tensor in their anisotropic damage model, in which they couple plastic deformation with damage induced by growth of microcracks. They also draw on the work of Pietruszczak in their formulation. They obtain good agreement with their model on the Tournemire shale data. This is an advanced model, allowing for the yield to depend on stress, scalar measure of plastic strain, density of microcracks, and a scalar anisotropy parameter, which represents the projection of a microstructure tensor on the current loading direction.

Chen et al [20] discuss the coupling between inherent and induced anisotropy in sedimentary rocks, using a fabric tensor to characterize anisotropic behavior. They obtain good agreement on shear stress vs. strain for the Tournemire shale data. This is also a very advanced model, which allows for friction coefficient and material cohesion for a family of weakness planes.

Hu et al [21] add the effect of water content to the anisotropic modeling. They provide calibration of model parameters and show good agreement with Tournemire argillite data for triaxial tests, except for volumetric strain vs. axial strain. Capillary pressure is introduced to describe the effect of the water content, using the effective stress concept. The model represents random microcracks by several families of parallel penny-shaped microcracks. The overall plastic strain is defined as an average weighted by microcrack density.

Lisjak et al [22] addresses brittle failure of anisotropic Opalinus Clay with a transversely isotropic constitutive model. Model parameters are calibrated with uniaxial compressive strength tests and Brazil disc tests. Their model shows good agreement with experimental data for maximum principal failure stress vs. confining pressure. With their FEM-DEM method, they are able to calculate crack patterns for various orientations.

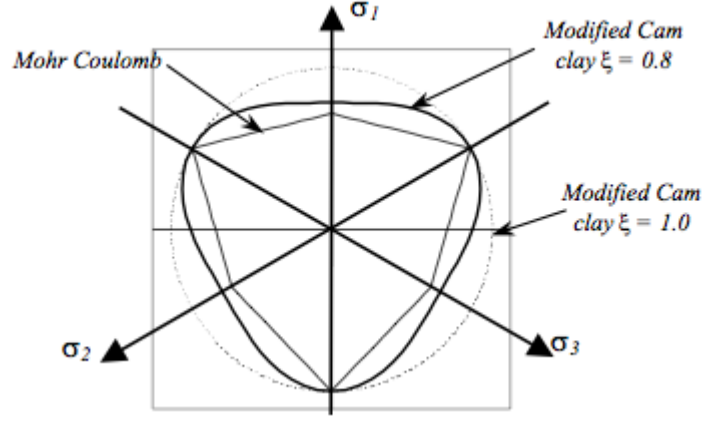


Figure 1: Adjusting yield surface for anisotropic shale [5]

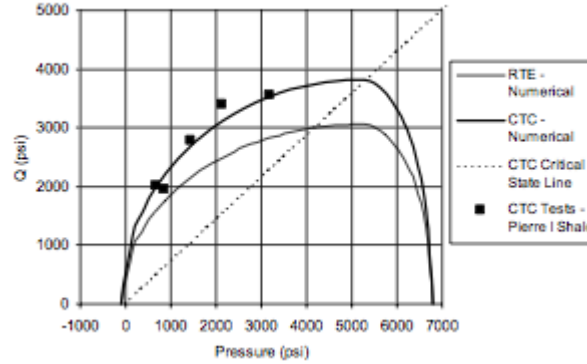


Figure 2: Equivalent stress vs. pressure for Modified Cam Clay model [5]

4 Crook Anisotropic Model

Crook et al [5] draw from the work of Cazacu and Pietruszczak and present a complete anisotropic model based on extending the isotropic modified Cam Clay critical state model to allow orthotropic elasticity, an orthotropic pressure dependent yield surface, and hardening/softening governed by the evolution of volumetric plastic strain. Triaxial compression tests are used to validate the model. The model is applied for prediction of equivalent stress q vs. axial/radial strain. The model is successful in predicting peak values but has difficulty with the subsequent release. Nevertheless, this model appears to be a good candidate for a first implementation, given what is attempted in the formulation, which avoids the complexity of Pietruszczak's approach. The same model has also been used by Soreide et al [3] to evaluate borehole stability, using Abaqus to implement the model. Crook et al realize that for induced anisotropy due to

oriented growth of microcracks, a fabric tensor with an evolution law are needed. This is not included in their model. See the work of Chen [20] above. The effect of pore fluid pressure will require using a formulation sensitive to anisotropy, as described by Carroll [23] and by Chen and Nur [24]. See also the work of Hu et al [21], above.

Crook et al have adapted the Modified Cam Clay model for shale. Figure 1 shows the modified Cam Clay yield surface, and Figure 2 shows the corresponding representation for equivalent stress vs. pressure, thus resulting in a good fit with experimental data. The material parameters are calibrated by back-analysis of uniaxial and triaxial tests. The elastic parameters are determined from conventional triaxial tests as follows. Young's modulus normal to bedding plane and out-of-plane Poisson's ratio are determined from triaxial tests with horizontal bedding planes. In-plane Young's modulus and Poisson's ratio are determined from triaxial tests with vertical bedding planes. Out-of-plane shear modulus is estimated from St. Venant's formula [14].

The modified Cam Clay yield surface requires four parameters: pre-consolidation pressure p_c , tensile intercept p_t , slope of critical state line M , and consolidation cap shape parameter β . The slope M is determined from the ratio of equivalent stress to pressure at constant plastic volume from triaxial compression and extension data. The pressures p_c and p_t are the positive and negative intercepts of the projection of the yield surface in pressure-equivalent stress space. From triaxial data for various void volumes (i.e. plastic volumetric strain), a linear fit is determined for the variation of p_c and p_t with plastic volume. The parameter β is chosen based on previous work with sandstone.

The transverse isotropic yield surface defines the failure criterion and requires three parameters which are determined from unconfined compressive strengths from triaxial tests with differing bedding plane orientations. The model is calibrated to fit the experiment at orientations of 0, 45, and 90 degrees.

Finally, a characteristic length scale is required in order to reproduce the correct dependence of strength on specimen size. This parameter is used to scale the inelastic strain and is typically the grain size of the shale. Crook et al set this parameter to 0.05 " in their work on Pierre shale.

5 Crook model formulation

5.1 Governing equations

For a given strain increment $\Delta\epsilon$ and the transversely isotropic elasticity matrix \mathbf{D}^E , write the trial stress (including stress at previous time step n and Jaumann stress flux) as (assume that stress is positive in compression as usual in rock mechanics):

$$\tilde{\sigma} = \sigma_n + \mathbf{D}^E \Delta\epsilon + (\mathbf{W}_{n+1} \sigma_n - \sigma_n \mathbf{W}_{n+1}) \Delta t \quad (2)$$

Since stress is positive in compression, the stress decomposition into volumetric pressure $p = \frac{1}{3} \text{tr}(\sigma)$ and deviatoric stress \mathbf{S} has the form:

$$\sigma = p\mathbf{1} + \mathbf{S} \quad (3)$$

so that:

$$\tilde{\sigma} = \sigma_n + \mathbf{D}^E \Delta\epsilon + (\mathbf{W}_{n+1} \mathbf{S}_n - \mathbf{S}_n \mathbf{W}_{n+1}) \Delta t \quad (4)$$

Note that the Jaumann stress rate $\hat{\sigma}_J$ is symmetric, i.e.:

$$\hat{\sigma}_J = \mathbf{W} \mathbf{S} - \mathbf{S} \mathbf{W} \quad (5)$$

$$\hat{\sigma}_J^T = \hat{\sigma}_J \quad (6)$$

If the trial stress does not violate the yield criterion given by Equ. 11 (i.e. $\Phi \leq 0$), then the new stress is the trial stress. Otherwise, an iterative solution will be required as described below. Each iterate for the stress at the new time step $n + 1$ takes the form:

$$\sigma_{n+1} = \tilde{\sigma} - \mathbf{D}^E \Delta\epsilon^P \quad (7)$$

$$\Delta\epsilon^P = (\Delta\lambda) \mathbf{N} \quad (8)$$

$$\mathbf{N} = \frac{\partial \Phi}{\partial \sigma} \quad (9)$$

$$\Delta\epsilon_v^P = \text{tr}(\Delta\epsilon^P) = \Delta\lambda \text{tr}(\mathbf{N}) \quad (10)$$

where the yield function $\Phi(\sigma, \epsilon_v^P)$ is given by:

$$\Phi(\sigma, \epsilon_v^P) = \frac{1}{M^2} (F_1(\sigma))^2 + \frac{1}{b^2} (F_2(p, \epsilon_v^P))^2 - a(\epsilon_v^P)^2 \quad (11)$$

where M is the critical state line slope, and $b = 1$ if $p \geq (p_t - a)$, and $b = \beta$ otherwise, β being a consolidation cap parameter.

In the Crook model, the solution state consists of the stress σ , the plastic volumetric strain increment $\Delta\epsilon_v^P$, and the flow multiplier increment $(\Delta\lambda)$ satisfying Eqs. 7, 10, and 11. These equations are now re-written to apply a Newton-Raphson iterative solution as given by Eqs. (33) and (34) in Crook's paper [5], in which the residuals \mathbf{Y}_1, Y_2, Y_3 associated respectively with Eqs.

7,10, and 11 are defined. The partial derivatives of these residuals are given below:

$$\frac{\partial \mathbf{Y}_1}{\partial \boldsymbol{\sigma}} = \mathbf{I} + (\Delta\lambda) \mathbf{D}^E \frac{\partial \mathbf{N}}{\partial \boldsymbol{\sigma}} \quad (12)$$

$$\frac{\partial \mathbf{Y}_1}{\partial (\Delta\epsilon_v^P)} = (\Delta\lambda) \mathbf{D}^E \frac{\partial \mathbf{N}}{\partial (\Delta\epsilon_v^P)} \quad (13)$$

$$\frac{\partial \mathbf{Y}_1}{\partial (\Delta\lambda)} = \mathbf{D}^E \mathbf{N} \quad (14)$$

$$\frac{\partial Y_2}{\partial \boldsymbol{\sigma}} = -(\Delta\lambda) \frac{\partial (\text{tr}(\mathbf{N}))}{\partial \boldsymbol{\sigma}} \quad (15)$$

$$\frac{\partial Y_2}{\partial (\Delta\epsilon_v^P)} = 1 - (\Delta\lambda) \frac{\partial (\text{tr}(\mathbf{N}))}{\partial (\Delta\epsilon_v^P)} \quad (16)$$

$$\frac{\partial Y_2}{\partial (\Delta\lambda)} = -\text{tr}(\mathbf{N}) \quad (17)$$

$$\frac{\partial Y_3}{\partial \boldsymbol{\sigma}} = \frac{1}{M^2} (2F_1 \frac{\partial F_1}{\partial \boldsymbol{\sigma}}) + \frac{2}{b^2} (F_2 \frac{\partial F_2}{\partial \boldsymbol{\sigma}}) \quad (18)$$

$$\frac{\partial Y_3}{\partial (\Delta\epsilon_v^P)} = \frac{2}{b^2} (F_2 \frac{\partial F_2}{\partial (\Delta\epsilon_v^P)}) - 2a \frac{\partial a}{\partial (\Delta\epsilon_v^P)} \quad (19)$$

$$\frac{\partial Y_3}{\partial (\Delta\lambda)} = 0 \quad (20)$$

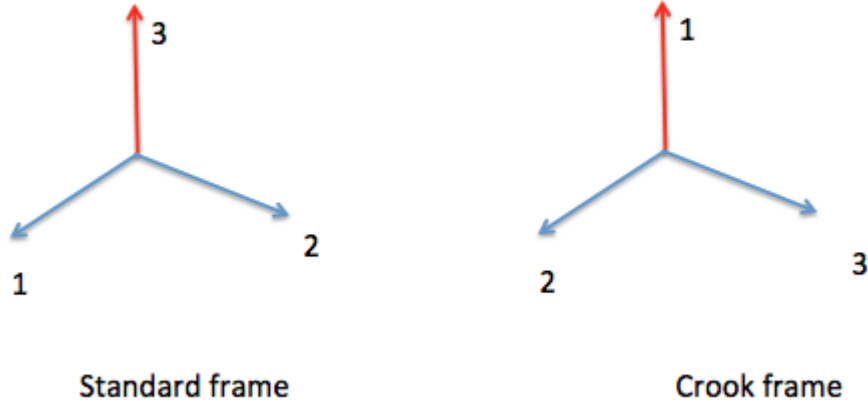


Figure 3: Transverse Isotropy Standard and Crook Frames

5.2 Elasticity matrix

The elasticity stiffness matrix D^E is given by Bower in [25] (p. 84) with respect to a standard frame, as shown in Figure 3. In this standard frame, the "1-2" plane is the isotropic bedding plane, while the "3" axis is normal to the bedding plane. Crook uses "2-3" for the isotropic bedding plane and the "1" axis normal to the bedding plane. Furthermore, in writing the stress-strain relation:

$$\sigma = D^E \epsilon \quad (21)$$

the stress and strain components are represented as vectors, following Voigt ordering: [11 22 33 23 13 12]. With the standard frame and the Voigt ordering, the elasticity matrix for transverse isotropy has the structure given by Bower [25] as:

$$D^E = \begin{pmatrix} D_{PS}^E & O \\ O & D_{GS}^E \end{pmatrix} \quad (22)$$

in which the subscript "P" refers to the part of the matrix relating [11 22 33] components, the subscript "G" refers to the part of the matrix relating [23 13 12] components, and the subscript "S" refers to the standard frame. Within the standard frame, elastic coefficients associated with the bedding plane will be labeled with the subscript "2" (interchangeable with subscript "1"). The subscript "3" will be associated with the transverse axis normal to the bedding

(isotropic) plane. Then, the components of D_{PS}^E are given by:

$$(D_{PS}^E)_{11} = (D_{PS}^E)_{22} = AE_2(1 - \nu_{23}\nu_{32}) \quad (23)$$

$$(D_{PS}^E)_{12} = AE_2(\nu_2 + \nu_{23}\nu_{32}) \quad (24)$$

$$(D_{PS}^E)_{13} = (D_{PS}^E)_{23} = AE_2\nu_{32}(1 + \nu_2) \quad (25)$$

$$(D_{PS}^E)_{33} = AE_3(1 - \nu_2^2) \quad (26)$$

$$A^{-1} = (1 - \nu_2 - 2\nu_{23}\nu_{32})(1 + \nu_2) \quad (27)$$

The other components follow by symmetry. In order for the stiffness matrix to be symmetric, the following must hold:

$$\frac{\nu_{32}}{E_3} = \frac{\nu_{23}}{E_2} \quad (28)$$

The components of D_{GS}^E are given by:

$$(D_{GS}^E)_{11} = (D_{GS}^E)_{22} = G_3 \quad (29)$$

$$(D_{GS}^E)_{33} = G_2 = \frac{E_2}{2(1 + \nu_2)} \quad (30)$$

All other components are zero. G_3 is given by St. Venant's formula [26] as:

$$\frac{1}{G_3} = \frac{1}{E_3} + \frac{1}{E_2} + 2\frac{\nu_{32}}{E_3} \quad (31)$$

While the elasticity matrix will be written with respect to the standard frame and the Voigt order, the coefficients will be interpreted with respect to the Crook frame, designated with subscript or superscript "C", as follows:

$$E_2 = E_2^C \quad (32)$$

$$E_3 = E_1^C \quad (33)$$

$$\nu_2 = \nu_{23}^C \quad (34)$$

$$\nu_{32} = \nu_{12}^C \quad (35)$$

$$\nu_{23} = \nu_{21}^C \quad (36)$$

$$G_2 = G_2^C \quad (37)$$

$$G_3 = G_1^C \quad (38)$$

The new form of the elasticity matrix becomes:

$$\mathbf{D}^E = \begin{pmatrix} D_{PC}^E & O \\ O & D_{GC}^E \end{pmatrix} \quad (39)$$

with components:

$$(D_{PC}^E)_{11} = (D_{PC}^E)_{22} = AE_2^C(1 - \nu_{21}^C \nu_{12}^C) \quad (40)$$

$$(D_{PC}^E)_{12} = AE_2^C(\nu_{23}^C + \nu_{21}^C \nu_{12}^C) \quad (41)$$

$$(D_{PC}^E)_{13} = (D_{PC}^E)_{23} = AE_2^C \nu_{12}^C(1 + \nu_{23}^C) \quad (42)$$

$$(D_{PC}^E)_{33} = AE_1^C(1 - (\nu_{23}^C)^2) \quad (43)$$

$$A^{-1} = (1 - \nu_{23}^C - 2\nu_{21}^C \nu_{12}^C)(1 + \nu_{23}^C) \quad (44)$$

$$(D_{GC}^E)_{11} = (D_{GC}^E)_{22} = G_{12}^C \quad (45)$$

$$(D_{GC}^E)_{33} = G_{23}^C = \frac{E_2^C}{2(1 + \nu_{23}^C)} \quad (46)$$

and the same constraints:

$$\frac{\nu_{12}^C}{E_1^C} = \frac{\nu_{21}^C}{E_2^C} \quad (47)$$

$$\frac{1}{G_{12}^C} = \frac{1}{E_1^C} + \frac{1}{E_2^C} + 2\frac{\nu_{12}^C}{E_1^C} \quad (48)$$

5.3 Construction of yield surface

Crook draws on work by Hashagen and Borst [27] who elaborate on the Hoffman criterion [28]. Hoffman uses a frame with x-y in the isotropic bedding plane and the z-axis normal to the bedding plane. This maps directly to the standard frame with "1-2" corresponding to "x-y" and "3" corresponding to "z". However, Hoffman does not use the Voigt order for stress, but instead σ^* with components ordered as [11 22 33 12 23 13] in the yield criterion given by Equ. 11, in which:

$$F_1(\sigma^*) = \frac{g(\theta)}{2} \sqrt{\frac{1}{2} \sigma^{*T} P_{orth} \sigma^*} \quad (49)$$

$$\theta = \frac{1}{3} \sin^{-1} \left(\frac{3\sqrt{3}}{2} \frac{J'_3}{(J'_2)^{3/2}} \right) \quad (50)$$

$$g(\theta) = [(1 + 1/\xi) - (1 - 1/\xi) \sin(3\theta)] \quad (51)$$

$$F_2(p, \epsilon_v^P) = p - p_t(\epsilon_v^P) + a(\epsilon_v^P) \quad (52)$$

where:

$$a(\epsilon_v^P) = \frac{1}{1 + \beta} (p_t(\epsilon_v^P) - p_c(\epsilon_v^P)) \quad (53)$$

$$(54)$$

The consolidation pressure is represented with a linear fit:

$$p_c(\epsilon_v^P) = p_{c0} + k_c \epsilon_v^P \quad (55)$$

The tensile cut-off pressure is represented with a linear fit:

$$p_t(\epsilon_v^P) = p_{t0} + k_t \epsilon_v^P \quad (56)$$

In the initial version of the code, the yield formulation has been simplified so that F_2 and a have the form:

$$F_2(p) = p \quad (57)$$

$$a = -p_{c0} \quad (58)$$

and the constant b in Eq. 11 is taken as 1.0. The yield in Eq. 11 thus takes the form:

$$\Phi(\sigma) = \left(\frac{g(\mathbf{S})}{2M} \right)^2 T(\sigma) + p^2 - (p_{c0})^2 \quad (59)$$

where $T(\sigma)$ is given by Eq. 111 and $g(\mathbf{S})$ is given by Eq. 107.

Crook uses the Cam-Clay parameter ξ to fit yield data, with ξ in the range

$$0.778 \leq \xi \leq 1.0.$$

$$\mathbf{P}_{orth} = \begin{pmatrix} \mathbf{\Omega}_{orth} & \mathbf{O} \\ \mathbf{O} & \mathbf{\Gamma}_{orth} \end{pmatrix} \quad (60)$$

$$\mathbf{\Omega}_{orth} = \begin{pmatrix} 4\alpha_4 & -2\alpha_4 & -2\alpha_4 \\ -2\alpha_4 & 2(\alpha_4 + \alpha_5) & -2\alpha_5 \\ -2\alpha_4 & -2\alpha_5 & 2(\alpha_4 + \alpha_5) \end{pmatrix} \quad (61)$$

$$\mathbf{\Gamma}_{orth} = \begin{pmatrix} 6\alpha_7 & 0 & 0 \\ 0 & 4(2\alpha_4 + \alpha_5) & 0 \\ 0 & 0 & 6\alpha_7 \end{pmatrix} \quad (62)$$

$$\boldsymbol{\sigma}^{*T} \mathbf{P}_{orth} \boldsymbol{\sigma}^* = \begin{pmatrix} Q_{11} & Q_{22} & Q_{33} & Q_{12} & Q_{23} & Q_{13} \end{pmatrix} \begin{pmatrix} \sigma_{11} \\ \sigma_{22} \\ \sigma_{33} \\ \sigma_{12} \\ \sigma_{23} \\ \sigma_{13} \end{pmatrix} \quad (63)$$

where:

$$Q_{11} = (\sigma_{11} \ \sigma_{22} \ \sigma_{33}) \begin{pmatrix} 4\alpha_4 \\ -2\alpha_4 \\ -2\alpha_4 \end{pmatrix} \quad (64)$$

$$Q_{22} = (\sigma_{11} \ \sigma_{22} \ \sigma_{33}) \begin{pmatrix} -2\alpha_4 \\ 2(\alpha_4 + \alpha_5) \\ -2\alpha_5 \end{pmatrix} \quad (65)$$

$$Q_{33} = (\sigma_{11} \ \sigma_{22} \ \sigma_{33}) \begin{pmatrix} -2\alpha_4 \\ -2\alpha_5 \\ 2(\alpha_4 + \alpha_5) \end{pmatrix} \quad (66)$$

$$Q_{12} = (\sigma_{12} \ \sigma_{23} \ \sigma_{13}) \begin{pmatrix} 6\alpha_7 \\ 0 \\ 0 \end{pmatrix} \quad (67)$$

$$Q_{23} = (\sigma_{12} \ \sigma_{23} \ \sigma_{13}) \begin{pmatrix} 0 \\ 4(2\alpha_4 + \alpha_5) \\ 0 \end{pmatrix} \quad (68)$$

$$Q_{13} = (\sigma_{12} \ \sigma_{23} \ \sigma_{13}) \begin{pmatrix} 0 \\ 0 \\ 6\alpha_7 \end{pmatrix} \quad (69)$$

6 Alternative scheme for keeping stress state approximately on yield surface

6.1 Approximate consistency criterion

The solution scheme described by Crook is appropriate to a fully implicit treatment of the governing equations. However, it does require laborious coding to calculate first and second derivatives of the yield criterion. Here, we will consider schemes that use only first derivatives and assume explicit integration with very small time steps. Following Borja [29], this approach should lead to nested one-dimensional Newton-Raphson iterations, requiring only first derivatives. For this purpose, the requirement that the stress and plastic volumetric strain remain on the yield surface will be addressed as a first step only by calculating the increment in the plastic multiplier $\Delta\lambda$ necessary to satisfy consistency, i.e. from the definition of the yield criterion in Equ. 9. Borja solves rigorously:

$$\Phi(\Delta\lambda, \boldsymbol{\sigma}, \epsilon_v^P) = 0 \quad (70)$$

for $\Delta\lambda$ such that the new stress and volumetric plastic strain lie on the updated yield surface. Given a trial state $(\tilde{\boldsymbol{\sigma}}, (\epsilon_v^P)_n)$ violating the yield criterion such that :

$$\Phi(\tilde{\boldsymbol{\sigma}}, (\epsilon_v^P)_n) > 0 \quad (71)$$

we will first attempt to solve the less rigorous:

$$\Phi(\tilde{\boldsymbol{\sigma}}, (\epsilon_v^P)_n) + \Delta\Phi(\Delta\lambda) = 0 \quad (72)$$

for $\Delta\lambda$ such that:

$$\Delta\Phi(\Delta\lambda) = \frac{\partial\Phi}{\partial\boldsymbol{\sigma}}\Delta\boldsymbol{\sigma} + \frac{\partial\Phi}{\partial\epsilon_v^P}\Delta\epsilon_v^P = -\Phi(\tilde{\boldsymbol{\sigma}}, (\epsilon_v^P)_n) \quad (73)$$

After the model has been implemented this far, Borja's more rigorous scheme will be considered. Other schemes, such as Jeremic's "midpoint rule" [30] will be considered later. So far, it appears that Jeremic's scheme requires second order derivatives.

Define:

$$\zeta = \frac{\partial\Phi}{\partial\epsilon_v^P} \quad (74)$$

and using Equ. 9, consistency requires:

$$\mathbf{N}^T\Delta\boldsymbol{\sigma} + \zeta\Delta\epsilon_v^P = -\Phi(\tilde{\boldsymbol{\sigma}}, (\epsilon_v^P)_n) \quad (75)$$

From Eqs. 4 through 10, define:

$$\Delta\boldsymbol{\sigma} = \boldsymbol{\sigma}_{n+1} - (\boldsymbol{\sigma}_n + (\mathbf{W}_{n+1}\mathbf{S}_n - \mathbf{S}_n\mathbf{W}_{n+1})\Delta t) \quad (76)$$

From Eqs. 10 and 75:

$$\mathbf{N}^T \Delta \boldsymbol{\sigma} + \zeta(\Delta \lambda) \text{tr}(\mathbf{N}) = -\Phi(\tilde{\boldsymbol{\sigma}}, (\epsilon_v^P)_n) \quad (77)$$

From Eqs. 4,7,8:

$$\Delta \boldsymbol{\sigma} = \mathbf{D}^E (\Delta \boldsymbol{\epsilon} - \Delta \lambda \mathbf{N}) \quad (78)$$

Substituting 78 into 77:

$$\mathbf{N}^T \mathbf{D}^E (\Delta \boldsymbol{\epsilon} - \Delta \lambda \mathbf{N}) + \zeta(\Delta \lambda) \text{tr}(\mathbf{N}) = -\Phi(\tilde{\boldsymbol{\sigma}}, (\epsilon_v^P)_n) \quad (79)$$

Solving for $\Delta \lambda$:

$$\Delta \lambda = \frac{\mathbf{N}^T \mathbf{D}^E \Delta \boldsymbol{\epsilon} + \Phi(\tilde{\boldsymbol{\sigma}}, (\epsilon_v^P)_n)}{\mathbf{N}^T \mathbf{D}^E \mathbf{N} - \zeta \text{tr}(\mathbf{N})} \quad (80)$$

6.2 Approximate numerical scheme

Given $\Delta \boldsymbol{\epsilon}$ and \mathbf{D}^E , the gradient \mathbf{N} will be evaluated at the trial stress $\tilde{\boldsymbol{\sigma}}$, and the derivative ζ will be evaluated with ϵ_v^P from the previous cycle. Given $\Delta \lambda$ from Equ. 93, the full plastic strain increment can then be calculated from Equ. 8 and its volumetric part from Equ. 10 which can be used to advance it:

$$(\epsilon_v^P)_{n+1} = (\epsilon_v^P)_n + \Delta \epsilon_v^P \quad (81)$$

We can then update the elastic strain increment from:

$$\Delta \boldsymbol{\epsilon}^E = \Delta \boldsymbol{\epsilon} - \Delta \boldsymbol{\epsilon}^P \quad (82)$$

and calculate a new estimate for the new stress as:

$$\boldsymbol{\sigma}_{n+1} = \boldsymbol{\sigma}_n + \mathbf{D}^E \Delta \boldsymbol{\epsilon}^E + (\mathbf{W}_{n+1} \mathbf{S}_n - \mathbf{S}_n \mathbf{W}_{n+1}) \Delta t \quad (83)$$

At this point we can check and report the error in satisfying the yield criterion by evaluating Equ. 11 at the new stress and plastic volumetric strain.

We now proceed to make this scheme iterative. First, we calculate quantities which need to be calculated only once for the entire simulation, namely the elastic matrix \mathbf{D}^E from Eqs. 40 through 46. Second, at each cycle, we calculate quantities that need to be calculated only once per cycle, namely: the deformation gradient \mathbf{D} and spin \mathbf{W} from Eqs. 126 and 127, the strain increment $\Delta \boldsymbol{\epsilon}$ from Eq. 128, an elastic stress increment $\Delta \boldsymbol{\sigma}^E$ from:

$$\Delta \boldsymbol{\sigma}^E = \mathbf{D}^E \Delta \boldsymbol{\epsilon} \quad (84)$$

and $\boldsymbol{\sigma}_o$ the sum of the old stress and the Jaumann increment from:

$$\boldsymbol{\sigma}_o = \boldsymbol{\sigma}_n + (\mathbf{W}_{n+1} \mathbf{S}_n - \mathbf{S}_n \mathbf{W}_{n+1}) \Delta t \quad (85)$$

To make this scheme iterative, proceed as follows: Let r designate the iteration counter. For $r = 0$, initialize the new iterate as:

$$(\boldsymbol{\sigma}_{n+1})^{(r)} = \tilde{\boldsymbol{\sigma}} \quad (86)$$

$$(\boldsymbol{\epsilon}_{n+1}^P)^{(r)} = (\boldsymbol{\epsilon}^P)_n \quad (87)$$

$$((\epsilon_v^P)_{n+1})^{(r)} = (\epsilon_v^P)_n \quad (88)$$

$$(89)$$

For successive iterations $r > 0$, initialize the new iterate as:

$$(\boldsymbol{\sigma}_{n+1})^{(r)} = (\boldsymbol{\sigma}_{n+1})^{(r-1)} \quad (90)$$

$$(\boldsymbol{\epsilon}_{n+1}^P)^{(r)} = (\boldsymbol{\epsilon}_{n+1}^P)^{(r-1)} \quad (91)$$

$$((\epsilon_v^P)_{n+1})^{(r)} = ((\epsilon_v^P)_{n+1})^{(r-1)} \quad (92)$$

During any iteration calculate:

1. $\zeta((\boldsymbol{\epsilon}_{n+1}^P)^{(r)})$ and $\mathbf{N}((\boldsymbol{\sigma}_{n+1})^{(r)}, (\boldsymbol{\epsilon}_{n+1}^P)^{(r)})$ from Eq. 100 through Eq. 125.
2. The yield $h^{(r)} = \Phi((\boldsymbol{\sigma}_{n+1})^{(r)}, ((\epsilon_v^P)_{n+1})^{(r)})$ from Eqs. 11, 50 through 52.
3. $\Delta\lambda$ from Eq. 93 and 84 so that:

$$\Delta\lambda = \frac{\mathbf{N}^T \Delta\boldsymbol{\sigma}^E + \Phi}{\mathbf{N}^T \mathbf{D}^E \mathbf{N} - \zeta \text{tr}(\mathbf{N})} \quad (93)$$

4. $(\Delta\boldsymbol{\epsilon}^P)^{(r+1)} = \Delta\lambda \mathbf{N}$
5. $(\boldsymbol{\epsilon}_{n+1}^P)^{(r+1)} = (\boldsymbol{\epsilon}^P)_n + (\Delta\boldsymbol{\epsilon}^P)^{(r+1)}$
6. $(\epsilon_v^P)_{n+1}^{(r+1)} = (\epsilon_v^P)_n + \Delta\lambda \text{tr}(\mathbf{N})$
7. $\Delta\boldsymbol{\epsilon}^E = \Delta\boldsymbol{\epsilon} - (\Delta\boldsymbol{\epsilon}^P)^{(r+1)}$
8. $(\boldsymbol{\sigma}_{n+1})^{(r+1)} = \boldsymbol{\sigma}_o + \mathbf{D}^E \Delta\boldsymbol{\epsilon}^E$

To check for convergence, calculate:

$$h^{(r+1)} = \Phi((\boldsymbol{\sigma}_{n+1})^{(r+1)}, ((\epsilon_v^P)_{n+1})^{(r+1)}) \quad (94)$$

6.3 Modified scheme using radial return

The above iterative scheme was found to require more than 50 iterations to converge. It also showed some instability at high strain rates. Therefore, an approach using radial return is explored as follows. From Eqs. 7 and 8:

$$\boldsymbol{\sigma}_{n+1} = \tilde{\boldsymbol{\sigma}} - (\Delta\lambda) \mathbf{D}^E \mathbf{N} \quad (95)$$

With radial return, a fraction γ of the trial stress is determined so that the yield vanishes. We consider so far the special case of constant yield strength given in Eq. 59, so that:

$$\Phi(\gamma \tilde{\boldsymbol{\sigma}}) = 0 \quad (96)$$

So that, whenever, $\Phi(\tilde{\boldsymbol{\sigma}}) > 0$, we can calculate:

$$\gamma = p_{c0} \left(\left(\frac{g(\tilde{\mathbf{S}})}{2M} \right)^2 T(\tilde{\boldsymbol{\sigma}}) + (\tilde{p})^2 \right)^{(-1/2)} \quad (97)$$

Then using the predicted reduced stress

$$\boldsymbol{\sigma}_{n+1} = \gamma \tilde{\boldsymbol{\sigma}} \quad (98)$$

as an estimate of the stress at the end of the time step and evaluating gradients at that estimate, we find:

$$\Delta\lambda = \frac{(1-\gamma)\mathbf{N}^T \tilde{\boldsymbol{\sigma}}}{\mathbf{N}^T \mathbf{D}^E \mathbf{N}} \quad (99)$$

6.4 Calculation of gradients

From Eqs. 11 and 52, since only F_2 depends on ϵ_v^P :

$$\zeta = \frac{\partial \Phi}{\partial \epsilon_v^P} = \frac{2}{b^2} F_2 \frac{\partial F_2}{\partial \epsilon_v^P} - 2a \frac{\partial a}{\partial \epsilon_v^P} \quad (100)$$

$$\frac{\partial F_2}{\partial \epsilon_v^P} = -p'_t(\epsilon_v^P) + a'(\epsilon_v^P) \quad (101)$$

The calculation of the gradient \mathbf{N} will be defined with respect to the stress components arranged in Voigt order, with the single index k ranging from 1 to 6 corresponding to [11 22 33 23 13 12].

$$N^k = \frac{\partial \Phi}{\partial \sigma^k} = \frac{2}{M^2} F_1 \frac{\partial F_1}{\partial \sigma^k} + \frac{2}{b^2} F_2 \frac{\partial F_2}{\partial p} \frac{\partial p}{\partial \sigma^k} \quad (102)$$

where, for $k = 1, 2, 3$:

$$\frac{\partial p}{\partial \sigma^k} = \frac{1}{3} \quad (103)$$

and, for $k = 4, 5, 6$:

$$\frac{\partial p}{\partial \sigma^k} = 0 \quad (104)$$

$$\frac{\partial F_2}{\partial p} = 1 \quad (105)$$

From Eq. 50:

$$F_1(\boldsymbol{\sigma}) = \frac{g(\mathbf{S})}{2} \sqrt{\frac{1}{2} \boldsymbol{\sigma}^T \mathbf{P}_V \boldsymbol{\sigma}} \quad (106)$$

$$g(\mathbf{S}) = [(1 + 1/\xi) - (1 - 1/\xi) \left(\frac{3\sqrt{3}}{2} \frac{J'_3(\mathbf{S})}{(J'_2(\mathbf{S}))^{3/2}} \right)] \quad (107)$$

where \mathbf{P}_V is derived from \mathbf{P}_{orth} in Eq. 60 by rearranging only the components of $\mathbf{\Gamma}_{orth}$ to follow Voigt order, so that, from Eq. 62:

$$\mathbf{\Gamma}_V = \begin{pmatrix} 4(2\alpha_4 + \alpha_5) & 0 & 0 \\ 0 & 6\alpha_7 & 0 \\ 0 & 0 & 6\alpha_7 \end{pmatrix} \quad (108)$$

$$\mathbf{\Omega}_V = \mathbf{\Omega}_{orth} \quad (109)$$

$$\mathbf{P}_V = \begin{pmatrix} \mathbf{\Omega}_V & \mathbf{O} \\ \mathbf{O} & \mathbf{\Gamma}_V \end{pmatrix} \quad (110)$$

Now define $T(\boldsymbol{\sigma})$ as:

$$T(\boldsymbol{\sigma}) = \frac{1}{2} \boldsymbol{\sigma}^T \mathbf{P}_V \boldsymbol{\sigma} \quad (111)$$

which, using Eq. 110, becomes:

$$T = \frac{1}{2} \left(\sum_{i=1}^3 \sum_{j=1}^3 \sigma^i \Omega_V^{ij} \sigma^j + \sum_{i=4}^6 \sum_{j=4}^6 \sigma^i \Gamma_V^{ij} \sigma^j \right) \quad (112)$$

$$\frac{\partial F_1}{\partial \sigma^m} = \frac{1}{2} \left(\frac{\partial g}{\partial S^k} \frac{\partial S^k}{\partial \sigma^m} \sqrt{T} + g \frac{\partial \sqrt{T}}{\partial \sigma^m} \right) \quad (113)$$

$$\frac{\partial g}{\partial S^k} = -(1 - 1/\xi) \left(\frac{3\sqrt{3}}{2} \right) ((-3/2) J'_3 (J'_2)^{-1/2} S^k + (J'_2)^{-3/2} \frac{\partial J'_3}{\partial S^k}) \quad (114)$$

$$J'_2 = (1/2)(S_1^2 + S_2^2 + S_3^2) + S_4^2 + S_5^2 + S_6^2 \quad (115)$$

$$J'_3 = S_1 S_2 S_3 + 2S_4 S_5 S_6 - S_1 S_4^2 - S_2 S_5^2 - S_3 S_6^2 \quad (116)$$

For $k = 1, 2, 3$ with (k, l, m) a cyclic permutation of 1, 2, 3:

$$\frac{\partial J'_3}{\partial S^k} = S^l S^m - (S^{k+3})^2 \quad (117)$$

$$\frac{\partial J'_3}{\partial S^{k+3}} = 2(S^{l+3} S^{m+3} - S^k S^{k+3}) \quad (118)$$

$$\frac{\partial \sqrt{T}}{\partial \sigma^m} = (1/4) \frac{R_m}{\sqrt{T}} \quad (119)$$

where, for $m = 1, 2, 3$:

$$R_m = 2 \sum_{i=1}^3 \Omega_V^{mi} \sigma^i \quad (120)$$

and for $m = 4, 5, 6$:

$$R_m = 2 \sum_{j=4}^6 \Gamma_V^{mj} \sigma^j \quad (121)$$

$$\frac{\partial S_{ij}}{\partial \sigma_{kl}} = (-1/3)\delta_{kl}\delta_{ij} + \delta_{ik}\delta_{jl} \quad (122)$$

from which:

$$B^{km} = \frac{\partial S^k}{\partial \sigma^m} \quad (123)$$

is given by:

$$\mathbf{B} = \begin{pmatrix} \mathbf{H} & \mathbf{O} \\ \mathbf{O} & \mathbf{I} \end{pmatrix} \quad (124)$$

where:

$$\mathbf{H} = \begin{pmatrix} (2/3) & (-1/3) & (-1/3) \\ (-1/3) & (2/3) & (-1/3) \\ (-1/3) & (-1/3) & (2/3) \end{pmatrix} \quad (125)$$

7 Implementation

The shale model has been implemented in C as a stand-alone software package. Currently, the model is exercised by specifying the velocity gradient at each cycle. Material response is output to a file.

7.1 Conventions

Since stress is positive in compression, and the velocity gradient \mathbf{L} is usually positive in tension, we have to calculate the strain increment to be positive in compression. Therefore:

$$\mathbf{d} = -(1/2)(\mathbf{L} + \mathbf{L}^T) \quad (126)$$

$$\mathbf{w} = -(1/2)(\mathbf{L} - \mathbf{L}^T) \quad (127)$$

$$\Delta\epsilon = \mathbf{d}\Delta t \quad (128)$$

Furthermore, all symmetric tensor quantities will be represented as a 6-component vector in Voigt order with the single index k ranging from 1 to 6 corresponding to [11 22 33 23 13 12].

7.2 Model parameters

7.2.1 Elasticity parameters input once

Young's modulus normal to bedding plane, E_1^C

Young's modulus within bedding plane, E_2^C

Poisson's ratio within bedding plane, ν_{23}^C

Poisson's ratio out-of-plane, ν_{12}^C

7.2.2 Derived elasticity parameters

Poisson's ratio ν_{21}^C derived using Eq. 47.

Out-of-plane shear modulus G_{12}^C derived using Eq. 48.

7.2.3 Plasticity parameters input once

Cam-clay parameter (dimensionless), ξ

Cap consolidation parameter (dimensionless), β

Critical state line slope (dimensionless), M

Orthotropic parameters (dimensionless), α_1 through α_8

Consolidation pressure p_{c0} (pressure units), Eq. 55.

8 Code verification

Since the current software is not yet part of a general hydro code allowing to apply the model on a mesh with boundary conditions and initial conditions, it is not yet possible to compare model results with experimental data. What can be done is to verify that the coding is consistent with the formulation documented above. This has been done for an isotropic test. For an anisotropic test, this has not been completed yet. However, we will compare an anisotropic calculation done with and without radial return.

8.1 Isotropic test

First consider a simple isotropic test. A single zone is subject to a constant compressive uniaxial strain rate $d_{11} = 10$ per ms applied for 1000 steps with time step $\Delta t = 10^{-7}$ ms. For the next 1000 steps, a tensile strain rate $d_{11} = -1$ per ms is applied to simulate unloading. Material parameters are chosen as follows. Both Young's moduli are taken to be equal to $E = 1000$ MPa. All Poisson's ratios are taken to be zero. In Eq. 59, take the parameter $M = 1$ and $p_{c0} = 0.1$ MPa. The yield is further simplified from Eq. 59, so that the parameter $\xi = 1$ in Eq. 52 for isotropic behavior and the matrix parameters Ω_V and Γ_V in Eqs. 61 and 62 are chosen so that all components vanish except for $\Omega_{V11} = 1$. The yield criterion then reduces to the form:

$$\phi = (1/2)(\sigma^1)^2 + p^2 - (p_{c0})^2 \quad (129)$$

Now proceed through the formulation and verify results calculated in the code, using a debugger. First calculate when yield first occurs. Until then, the pressure is given by:

$$p = (1/3)\sigma^1 \quad (130)$$

With a constant elastic stress increment

$$Ed_{11}\Delta t = 10^{-3} \quad (131)$$

calculate the number of steps when the yield first becomes positive. Combining above results, the yield after K cycles (noting that the first cycle is $K=0$) is given by:

$$\phi(K) = (11/18)(\sigma^1)^2 - (p_{c0})^2 = (11/18)10^{-3}(K+1)^2 - (p_{c0})^2 \quad (132)$$

giving $K=127$ when the yield first becomes positive, so that the trial stress $\tilde{\sigma}^1$ is 0.128 MPa, as verified in the code. Next, find the radial return fraction γ for bringing the stress to the yield surface. Solve

$$\phi(\gamma\sigma^1) = 0 \quad (133)$$

requiring:

$$(11/18)(\gamma\sigma^1)^2 - (p_{c0})^2 = 0 \quad (134)$$

giving $\gamma = 0.999378358$ verified in the code, as shown as "radRetFrac" in Figure 4. The reduced trial stress $\gamma\sigma^1 = 0.12792043$ is reproduced in Figure 4 as "strRet1". Now, in preparation for calculating $\Delta\lambda$, evaluate the stress gradients at this reduced trial stress, given by applying Eq. 102 to the simplified yield in Eq. 129:

$$N^1 = \frac{\partial\phi}{\partial\sigma^1} = \sigma^1 + (2/3)p = (11/9)\sigma^1 \quad (135)$$

$$N^2 = \frac{\partial\phi}{\partial\sigma^2} = (2/3)p = (2/9)\sigma^1 \quad (136)$$

$$N^3 = N^2 \quad (137)$$

Using the reduced stress:

$$N^1 = 0.156347192 \quad (138)$$

$$N^3 = N^2 = 0.028426762 \quad (139)$$

which all agree with the code as shown in Figure 4. Now proceed with the calculation of $\Delta\lambda$ from Eq. 99. First the numerator:

$$(1 - \gamma)\mathbf{N}^T \tilde{\boldsymbol{\sigma}} = (1 - \gamma)N^1\tilde{\sigma}^1 = 1.244057385 \times 10^{-5} \quad (140)$$

which agrees with Figure 4. Then, for the denominator, first form the product of the elasticity matrix with the gradients. For isotropic material, the elasticity matrix is reduced a diagonal form with the single Young's modulus. Multiplying the modulus by each gradient clearly gives what is shown in Figure 4 as DEN1, DEN2, DEN3. Finally, forming the dot product of the gradient vector with the previous result gives the value 26.060606 which agrees with Figure 4. The ratio of the numerator to the denominator gives $\Delta\lambda$ as $4.77370858 \times 10^{-7}$ which agrees with "dlambda" as shown in Figure 4. Now proceed with the calculation of plastic strain increments following Eq. 8, giving:

$$\Delta\epsilon^{P1} = \Delta\lambda N^1 = 7.46356 \times 10^{-8} \quad (141)$$

$$\Delta\epsilon^{P2} = \Delta\lambda N^2 = 1.3570108 \times 10^{-8} \quad (142)$$

$$\Delta\epsilon^{P3} = \Delta\epsilon^{P2} \quad (143)$$

all of which agree with "delplastrn1",2,3 shown in Figure 5. Now, since the total strain arises only from the applied strain rate in the 1-direction, the calculation of elastic strain increments will now show tensile reactions in the 2 and 3 directions equal and opposite to the plastic strain increments, thus giving rise to tensile stresses in the bedding plane. In Figure 7, this explains why the bedding stresses are tensile and become more so during the plastic phase. During elastic unloading, the plastic strain (see Figure 6) is fixed, so that there is no further change in the bedding stresses. Figure 8 shows that the yield criterion is satisfied, remaining close to zero, during the plastic phase, and staying negative during the elastic loading and unloading phases. One may ask whether the bedding stresses would be different if Poisson's ratio were not zero. Figure


```

block "$b1":
  N1: 1.563471919941143e-01
  N2: 2.842676218074806e-02
  N3: 2.842676218074806e-02
  N4: 0.000000000000000e+00
  N5: 0.000000000000000e+00
  N6: 0.000000000000000e+00
  zeta: 0.000000000000000e+00
  yieldFunc: 1.001244444444446e-02
  radRetFrac: 9.993783579169232e-01
  strRet1: 1.279204298133663e-01
  strRet2: 0.000000000000000e+00
  strRet3: 0.000000000000000e+00
  strRet4: 0.000000000000000e+00
  strRet5: 0.000000000000000e+00
  strRet6: 0.000000000000000e+00
  NdsigE: 1.563471919941143e-04
  DEN1: 1.563471919941143e+02
  DEN2: 2.842676218074806e+01
  DEN3: 2.842676218074806e+01
  DEN4: 0.000000000000000e+00
  DEN5: 0.000000000000000e+00
  DEN6: 0.000000000000000e+00
  NDEV: 2.606060606060606e+01
  zetaTrN: 0.000000000000000e+00
  NdotTrialStr: 2.001244057524664e-02
  numerator: 1.244057524664702e-05
  denom: 2.606060606060606e+01
  dlambda: 4.773709106271529e-07

```

Figure 4: debugger data for isotropic test with zero Poisson ratio

```

pc0: 1.000000000000000e-01
pc1: 1.000000000000000e-01
pc2: 1.000000000000000e-01
pt0: 0.000000000000000e+00
pt1: 0.000000000000000e+00
pt2: 0.000000000000000e+00
M: 1.000000000000000e+00
beta: 1.000000000000000e+00
Dpc11: 1.000000000000000e+03
Dpc22: 1.000000000000000e+03
Dpc33: 1.000000000000000e+03
Dpc23: 0.000000000000000e+00
Dpc13: 0.000000000000000e+00
Dpc12: 0.000000000000000e+00
Dgc11: 5.000000000000000e+02
Dgc22: 5.000000000000000e+02
Dgc33: 5.000000000000000e+02
yieldPrev: 1.2444444444445728e-05
yieldNext: 0x7fffffff4300 -> 6.953355807276;
block "$b1":
  delasStrn1: 9.253643985837713e-07
  delasStrn2: -1.357010934840521e-08
  delasStrn3: -1.357010934840521e-08
  delasStrn4: -0.000000000000000e+00
  delasStrn5: -0.000000000000000e+00
  delasStrn6: -0.000000000000000e+00
  delplastrn1: 7.463560141622867e-08
  delplastrn2: 1.357010934840521e-08
  delplastrn3: 1.357010934840521e-08
  delplastrn4: 0.000000000000000e+00
  delplastrn5: 0.000000000000000e+00
  delplastrn6: 0.000000000000000e+00
  dsigElas1: 9.253643985837713e-04
  dsigElas2: -1.357010934840521e-05
  dsigElas3: -1.357010934840521e-05
  dsigElas4: -0.000000000000000e+00
  dsigElas5: -0.000000000000000e+00
  dsigElas6: -0.000000000000000e+00

```

Figure 5: debugger plastic strain data for isotropic test with zero Poisson ratio

9 shows that, with Poisson ratio = 0.3, during the initial elastic loading phase, the bedding stresses are compressive, but the plastic phase brings on a tensile trend.

8.2 Anisotropic verification

Next consider an anisotropic test. A single zone is subject to a constant compressive uniaxial strain rate $d_{11} = 10$ per ms applied for 12 steps (sufficient to reach a plastic state) with time step $\Delta t = 10^{-6}$ ms. The goal will be to verify the initial elastic response cycle and the first plastic response cycle. So far only the elastic cycle has been completed.

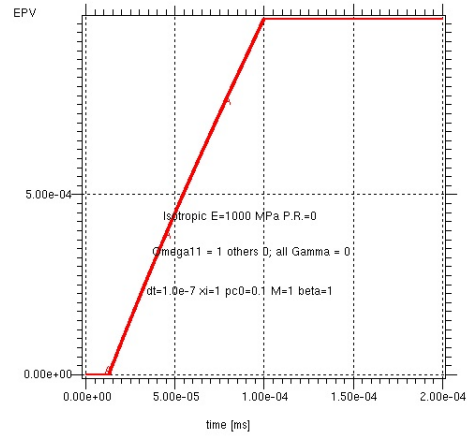


Figure 6: Volumetric plastic strain for isotropic test with zero Poisson ratio

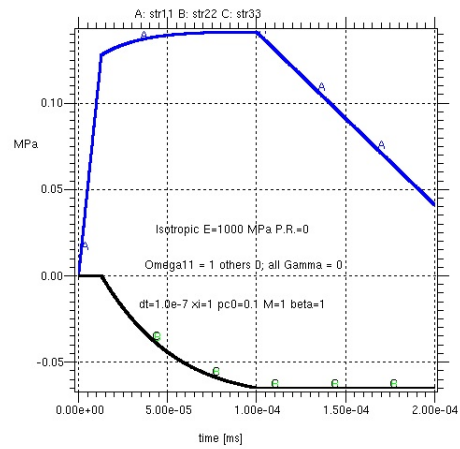


Figure 7: Stresses for isotropic test with zero Poisson ratio

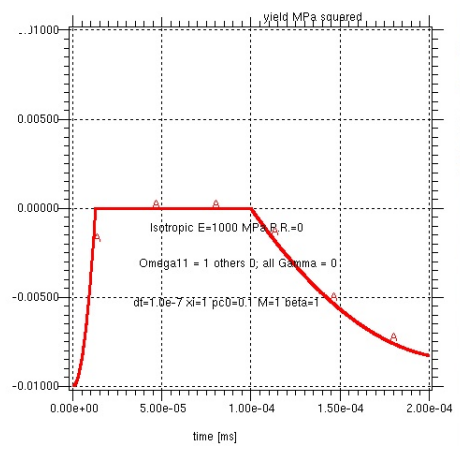


Figure 8: Yield for isotropic test with zero Poisson ratio

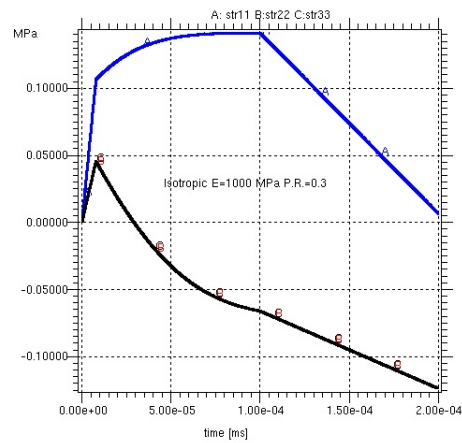


Figure 9: Stresses for isotropic test with positive Poisson ratio

8.2.1 Material parameters

$$E_1^C = 1500 \quad (144)$$

$$E_2^C = 2000 \quad (145)$$

$$\nu_{23}^C = 0.3 \quad (146)$$

$$\nu_{12}^C = 0.3 \quad (147)$$

$$\xi = 0.8 \quad (148)$$

$$M = 0.8 \quad (149)$$

$$\beta = 1.0 \quad (150)$$

$$\alpha_4 = \alpha_5 = 0.5 \quad (151)$$

$$\alpha_7 = 1.0 \quad (152)$$

$$\alpha_8 = \alpha_9 = 2.0 \quad (153)$$

$$p_{c0} = 0.25 \quad (154)$$

8.2.2 Elastic cycle

Applying Eqs. 40 through 48 gives:

$$\nu_{21} = 0.4 \quad (155)$$

$$G_{12} = 638.2978 \quad (156)$$

$$G_{23} = 769.23 \quad (157)$$

$$(158)$$

$$D_{PC}^E = \begin{pmatrix} (2943.14) & (1404.68) & (1304.35) \\ (1404.68) & (2943.14) & (1304.35) \\ (1304.35) & (1304.35) & (2282.61) \end{pmatrix} \quad (159)$$

$$D_{GC}^E = \begin{pmatrix} 638.30 & 0 & 0 \\ 0 & 638.30 & 0 \\ 0 & 0 & 769.23 \end{pmatrix} \quad (160)$$

All of the above values agree with the code as shown in Figure 10.

8.3 Anisotropic calculations with and without radial return

As mentioned in Section 6.3, the first scheme attempted, which did not use radial return, required more than 50 iterations to converge. By introducing radial return, a single iteration produced essentially the same results as the multi-iterative scheme. This is shown in Figures 11, 12, and 13.

```

E10: 1.500000000000000e+03
E20: 2.000000000000000e+03
nu120: 3.000000000000000e-01
nu210: 4.000000000000000e-01
nu230: 3.000000000000000e-01
G120: 6.382978723404256e+02
G230: 7.692307692307692e+02
xi: 8.000000000000000e-01
M: 8.000000000000000e-01
beta: 1.000000000000000e+00
alpha1: 3.333333333333333e-01
alpha2: 3.333333333333333e-01
alpha3: 3.333333333333333e-01
alpha4: 5.000000000000000e-01
alpha5: 5.000000000000000e-01
alpha6: 5.000000000000000e-01
alpha7: 1.000000000000000e+00
alpha8: 2.000000000000000e+00
alpha9: 2.000000000000000e+00
omega11: 2.000000000000000e+00
omega22: 2.000000000000000e+00
omega33: 2.000000000000000e+00
omega23: -1.000000000000000e+00
omega13: -1.000000000000000e+00
omega12: -1.000000000000000e+00
gammaa11: 6.000000000000000e+00
gammaa22: 6.000000000000000e+00
gammaa33: 6.000000000000000e+00
Dpc11: 2.943143812709030e+03
Dpc22: 2.943143812709030e+03
Dpc33: 2.282608695652174e+03
Dpc23: 1.304347826086957e+03
Dpc13: 1.304347826086957e+03
Dpc12: 1.404682274247492e+03
Dgc11: 6.382978723404256e+02
Dgc22: 7.692307692307692e+02
Dgc33: 7.692307692307692e+02
pc0: 2.500000000000000e-01

```

Figure 10: debugger data for elasticity matrix

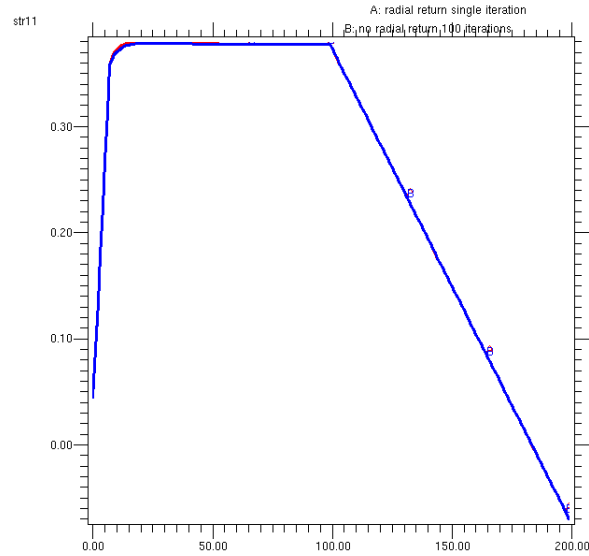


Figure 11: Anisotropic stress-11 response with and without radial return

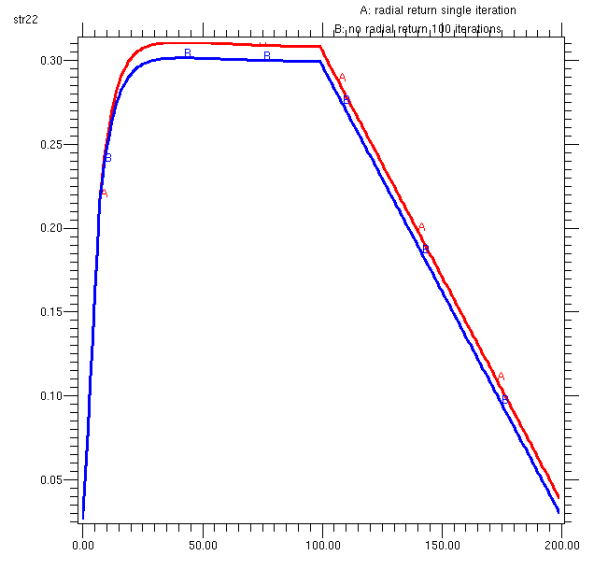


Figure 12: Anisotropic stress-22 response with and without radial return

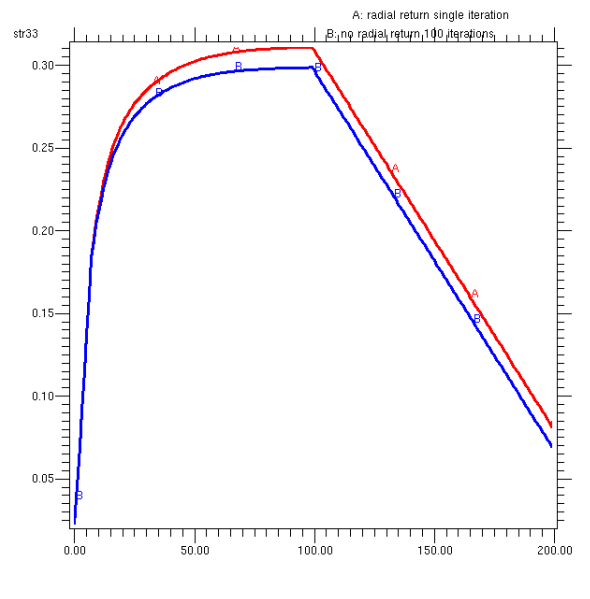


Figure 13: Anisotropic stress-33 response with and without radial return

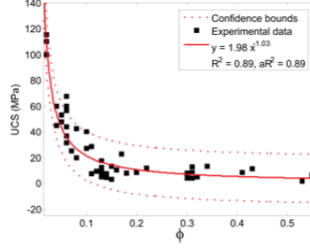


Figure 14: UCS vs. Porosity [31]

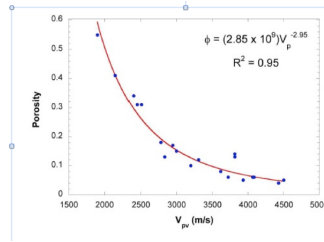


Figure 15: P-wave velocity vs. Porosity [31]

9 Sample properties from literature

Dewhurst et al [31] provide several interesting correlations of shale properties from a variety of geographical locations. Figure 14 shows correlation between unconfined compressive strength and porosity. Figure 15 shows a tight correlation between P-wave velocity and porosity.

Sone et al [32] provide properties of Barnett and Haynesville shale. Figure 16 shows sample mineral composition, frictional coefficients, unconfined compressive strengths. Figure 17 shows Young's modulus and Poisson's ratio.

Li et al [33] give shale strength data for Haynesville site. Figure 18 shows the effect of confining pressure on shale strength.

Sample Group	Qtz/Felds [%]	Carbonate [%]	Clay [%]	Others [%]	Pc Triax [MPa]	Creep Stress 1 st /2 nd step [MPa]	Frictional Coefficient	UCS [MPa]
Barnett Dark	60	10	25	5	30	-	0.923	160
					30	46.5 / 92.0	0.805	
					30	46.5 / 92.1	0.706	
					20	47.3 / 95.2	0.899	
					30	-	0.896	
					40	49.2 / 94.9	0.791	
Barnett Light	35	55	5	5	30	-	0.928	220
					20	44.7 / 89.7	1.10	
					40	48.6 / 94.0	-	
Haynesville Dark	45	13	39	3	60	-	0.534	120
					60	29.4 / 58.4	0.539	
					30	32.1 / 61.0	0.599	
					20	31.0 / 60.0	0.686	
					30	35.5 / 64.6	0.643	
Haynesville Light	28	48	22	2	60	-	0.675	160
					30	37.1 / 77.1	0.745	
					20	34.4 / 74.6	0.822	

Figure 16: Sample mineral composition and mechanical properties [32]

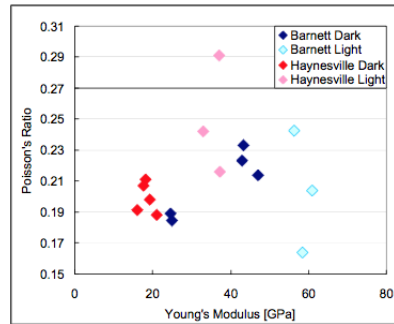


Figure 17: Sample Young's modulus and Poisson ratio [32]

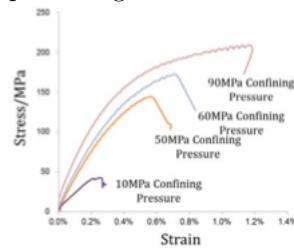


Figure 18: Effect of confining pressure on shale strength [33]

This work was performed under the auspices of the U.S. Department of Energy by Lawrence Livermore National Laboratory under Contract DE-AC52-07NA27344.

References

- [1] Aadnoy B. Modeling of the stability of highly inclined boreholes in anisotropic rock formations (includes associated papers 19213 and 19886). *SPE drilling engineering* 1988; **3**(3):259–268.
- [2] Cazacu O, Shao J, Henry J, Cristescu N. Elastic/viscoplastic constitutive equation for anisotropic shale. *2nd North American Rock Mechanics Symposium*, 1996.
- [3] Søreide O, Bostrøm B, Horsrud P. Borehole stability simulations of an hpht field using anisotropic shale modeling. *Proceedings of the ARMA conference, Asheville, North Carolina*, 2008.
- [4] Aoki T, Tan C, T COX R, Bamford W. Determination of anisotropic poroelastic parameters of a transversely isotropic shale by means of consolidated undrained triaxial tests. *8th ISRM Congress*, 1995.
- [5] Crook A, Jian-Guo Y, Willson S. Development of an orthotropic 3d elastoplastic material model for shale. *SPE/ISRM Rock Mechanics Conference*, 2002.
- [6] Islam M, Skalle P, Al-Ajmi A, Søreide O. Stability analysis in shale through deviated boreholes using the mohr and mogi-coulomb failure criteria. *44th US Rock Mechanics Symposium and 5th US Canada Rock Mechanics Symposium*, 2010.
- [7] Grady D, Kipp M. Continuum modelling of explosive fracture in oil shale. *International Journal of Rock Mechanics and Mining Sciences & Geomechanics Abstracts*, vol. 17, Elsevier, 1980; 147–157.
- [8] Kipp M, Grady D. Numerical studies of rock fragmentation. *Technical Report*, Sandia Labs., Albuquerque, NM (USA) 1980.
- [9] Kipp M, Grady D, Chen E. Strain-rate dependent fracture initiation. *International Journal of Fracture* 1980; **16**(5):471–478.
- [10] Taylor LM, Chen EP, Kuszmaul JS. Microcrack-induced damage accumulation in brittle rock under dynamic loading. *Computer Methods in Applied Mechanics and Engineering* 1986; **55**(3):301–320.
- [11] Zhang YQ, Hao H, Lu Y. Anisotropic dynamic damage and fragmentation of rock materials under explosive loading. *International Journal of Engineering Science* 2003; **41**(9):917–929.
- [12] Nova R. An extended cam clay model for soft anisotropic rocks. *Computers and Geotechnics* 1986; **2**(2):69–88.

- [13] Niandou H, Shao J, Henry J. Anisotropic yield and failure of shale. *Assessment and Prevention of Failure Phenomena in Rock Engineering: Proceedings of the International Symposium on Assessment and Prevention of Failure Phenomena in Rock Engineering: Istanbul, Turkey, 5-7 April 1993*, Taylor & Francis, 1993; 107.
- [14] Niandou H, Shao J, Henry J, Fourmaintraux D. Laboratory investigation of the mechanical behaviour of tournemire shale. *International Journal of Rock Mechanics and Mining Sciences* 1997; **34**(1):3–16.
- [15] Cazacu O, Cristescu N. A paraboloid failure surface for transversely isotropic materials. *Mechanics of materials* 1999; **31**(6):381–393.
- [16] Tien YM, Kuo MC. A failure criterion for transversely isotropic rocks. *International Journal of Rock Mechanics and Mining Sciences* 2001; **38**(3):399–412.
- [17] Pietruszczak S, Lydzba D, Shao JF. Modelling of inherent anisotropy in sedimentary rocks. *International journal of solids and structures* 2002; **39**(3):637–648.
- [18] Gao Z, Zhao J, Yao Y. A generalized anisotropic failure criterion for geomaterials. *International Journal of Solids and Structures* 2010; **47**(22):3166–3185.
- [19] Chen L, Shao JF, Huang H. Coupled elastoplastic damage modeling of anisotropic rocks. *Computers and Geotechnics* 2010; **37**(1):187–194.
- [20] Chen L, Shao J, Zhu Q, Duveau G. Induced anisotropic damage and plasticity in initially anisotropic sedimentary rocks. *International Journal of Rock Mechanics and Mining Sciences* 2012; **51**:13–23.
- [21] Hu D, Zhou H, Zhang F, Shao J, JF Z, *et al.*. Modeling of inherent anisotropic behavior of partially saturated clayey rocks. *Computers and Geotechnics* 2013; **48**:29–40.
- [22] Lisjak A, Tatone BS, Grasselli G, Vietor T. Numerical modelling of the anisotropic mechanical behaviour of opalinus clay at the laboratory-scale using fem/dem. *Rock Mechanics and Rock Engineering* 2012; :1–20.
- [23] Carroll M. An effective stress law for anisotropic elastic deformation. *Journal of Geophysical Research: Solid Earth (1978–2012)* 1979; **84**(B13):7510–7512.
- [24] Chen Q, Nur A. Pore fluid pressure effects in anisotropic rocks: mechanisms of induced seismicity and weak faults. *pure and applied geophysics* 1992; **139**(3-4):463–479.
- [25] Bower AF. *Applied mechanics of solids*. CRC press, 2011.

- [26] Saint Venant B. Sur la distribution des élasticités autour de chaque point d'un solide ou d'un milieu de contexture quelconque, particulièrement lorsqu'il est amorphe sans être isotrope. *Journal de Math. Pures et Appliquées* 1863; :257–430.
- [27] Hashagen F, De Borst R. Enhancement of the hoffman yield criterion with an anisotropic hardening model. *Computers & Structures* 2001; **79**(6):637–651.
- [28] Hoffman O. The brittle strength of orthotropic materials. *Journal of Composite Materials* 1967; **1**(2):200–206.
- [29] Borja RI, Lee SR. Cam-clay plasticity, part 1: implicit integration of elastoplastic constitutive relations. *Computer Methods in Applied Mechanics and Engineering* 1990; **78**(1):49–72.
- [30] Jeremic B. Eci289e computational geomechanics, inelastic finite elements for pressure sensitive materials. *Technical Report*, UC Davis, jeremic@ucdavis.edu 2002.
- [31] Dewhurst DN, Sarout JN, Piane CD, Siggins AF, Raven MD, Kuila UN. Prediction of shale mechanical properties from global and local empirical correlations. *2010 SEG Annual Meeting*, 2010.
- [32] Sone H, Zoback M. Strength, creep and frictional properties of gas shale reservoir rocks. *44th US Rock Mechanics Symposium and 5th US-Canada Rock Mechanics Symposium*, 2010.
- [33] Li Q, Chen M, Jin Y, Zhou Y, Wang F, Zhang R. Rock mechanical properties of shale gas reservoir and their influences on hydraulic fracture. *IPTC 2013: International Petroleum Technology Conference*, 2013.